Helium-ion microscopy, helium-ion irradiation and nanoindentation of Eurofer 97 and ODS Eurofer

Bergner, F.; Hlawacek, G.; Heintze, C.;

Originally published:

May 2018

Journal of Nuclear Materials 505(2018), 267-275

DOI: https://doi.org/10.1016/j.jnucmat.2017.07.054

Perma-Link to Publication Repository of HZDR:

https://www.hzdr.de/publications/Publ-24323

Helium-ion microscopy, helium-ion irradiation and nanoindentation of Eurofer 97 and ODS Eurofer

F. Bergner*, G. Hlawacek, C. Heintze

Helmholtz-Zentrum Dresden-Rossendorf, Bautzner Landstraße 400, 01328 Dresden, Germany

Abstract

Understanding of unsolved details of helium embrittlement requires experimental evidence for dedicated sets of materials and over a wide range of irradiation conditions. The study is focussed on the comparison of the reduced-activation ferritic-martensitic 9%Cr steel with its oxide dispersion strengthened (ODS) counterpart with respect to irradiation-induced hardening. Imaging and He-ion irradiation in the He-ion microscope at 30 ºC in a wide range of appm He (from 0.9 x 10^2 to 1.8 x 10^6) and displacements per atom (from 3 x 10^{-3} to 65) were combined with post-irradiation nanoindentation in order to detect blistering and irradiation-induced hardness changes. The applicability of this combination of techniques is demonstrated and pros and cons are discussed. We have found that the irradiation-induced hardness increase is higher and the onset of significant hardening tends to occur at lower fluence for Eurofer 97 than for ODS Eurofer, indicating that the presence of oxide nanoparticles is efficient to reduce the detrimental effect of He under the applied irradiation conditions.

Keywords: Ferritic-martensitic chromium steel, Oxide dispersion strengthened steel, He-ion microscopy, Ion irradiation, Nanoindentation

1 Introduction

He embrittlement of steels has been attracting much attention since mid-‘60s, when Barnes [1] attributed high temperature embrittlement of irradiated steels to helium bubbles in grain boundaries. A popular introduction into the subject was given by Ullmaier in 1982 [2] on the occasion of an International Symposium on “Fundamental Aspects of Helium in Metals”. While a broad understanding of He-related phenomena in irradiated materials is available by now [3], current research interest is focussed on details required for both comprehensive multiscale modelling and the development of irradiation-resistant structural materials [4,5]. At the same time, experimental access to the formation and evolution of He bubbles is limited and evidence from experimental investigations is still incomplete [6].

* Corresponding author. Tel.: +49 351 260 3186; fax: +49 351 260 2205.
E-mail address: f.bergner@hzdr.de (F. Bergner).

Ferritic-martensitic (f/m) high-Cr steels including their reduced-activation variants as well as advanced oxide dispersion strengthened (ODS) steels, also referred to as nanostructured ferritic or transformable (ferritic-martensitic) steels, are candidate structural materials for various nuclear applications. These include the first wall blanket of the demonstration (DEMO) fusion reactor [7], the beam window of accelerator driven systems (ADS) [8] as well as fuel pin cladding tubes of sodium fast reactors (SFR) [9]. Regarding He management, advanced ODS steels are believed to be superior over monolithic f/m steels due to the operation of oxide-matrix interfaces as He traps preventing He from accumulating at grain boundaries [4,5] and giving rise to grain boundary embrittlement.

He ion microscopy (HIM), although a derivative of early field ion microscopy, has become available only recently, after technical issues had been solved [10]. There is a growing field of applications in materials science not only for the purpose of high-resolution imaging but also for nanofabrication [11]. Occasionally, HIM has been applied as a means to intentionally introduce He into structural materials or model alloys [12,13]. This idea is adopted here in order to compare the low-activation f/m steel Eurofer 97 and its ODS counterpart with respect to the hardening caused by He-ion irradiation.

The study covers two distinct aims:

- First, it represents an attempt to combine HIM and nanoindentation in order to evaluate hardness changes induced by He-ion irradiation. In this respect, the study is aimed to explore possibilities and limitations inherent to this combination of methods.
- Second, the question will be answered if the irradiation response of ODS Eurofer differs significantly from Eurofer 97 under the specific irradiation conditions provided by HIM.

It is important to note that an additional question will automatically be addressed, although not conclusively solved, by way of pursuing the above aims, namely whether or not and up to which degree the imaging mode of HIM may give rise to He-related artefacts.

2 Experiments

2.1 Materials and samples

The ferritic/martensitic 9%Cr steel Eurofer 97 and ODS Eurofer were investigated. Eurofer 97 is a type 9Cr-1WVTa low-activation steel produced by Böhler Edelstahl AG, Kapfenberg, Austria. The 14 mm plate was treated at 980 °C for 27 min followed by air cooling [14]. Tempering was performed at 760 °C for 90 min. The composition is given in Table 1. The as-received material consists of tempered martensite. An inverse pole figure map obtained by means of electron backscatter diffraction (EBSD) is shown in Fig. 1(a) [15].

Table 1 Composition of Eurofer 97 (analysis, mass%, balance Fe).

Material	Cr	C	Mn	Si	P	S	V	W	Ta	Mo	Ni
Eurofer 97	8.82	0.11	0.47	0.04	0.005	0.004	0.2	1.09	0.13	<0.001	0.02

The ODS Eurofer provided by KIT, Karlsruhe, Germany, was produced from gas-atomized Eurofer 97 powder and 0.3 wt% Y_2O_3 powder by attritor milling and compacted by hot isostatic pressing followed by hot rolling to 6 mm thickness plates [16]. The plates were treated at 1100 °C for 30 min followed by water quenching and tempered at 750 °C for 2 h. The EBSD inverse pole figure map shown in Fig. 1**Fehler! Verweisquelle konnte nicht gefunden werden.**(b) [15] indicates finer grains than for Eurofer 97 (Table 2).

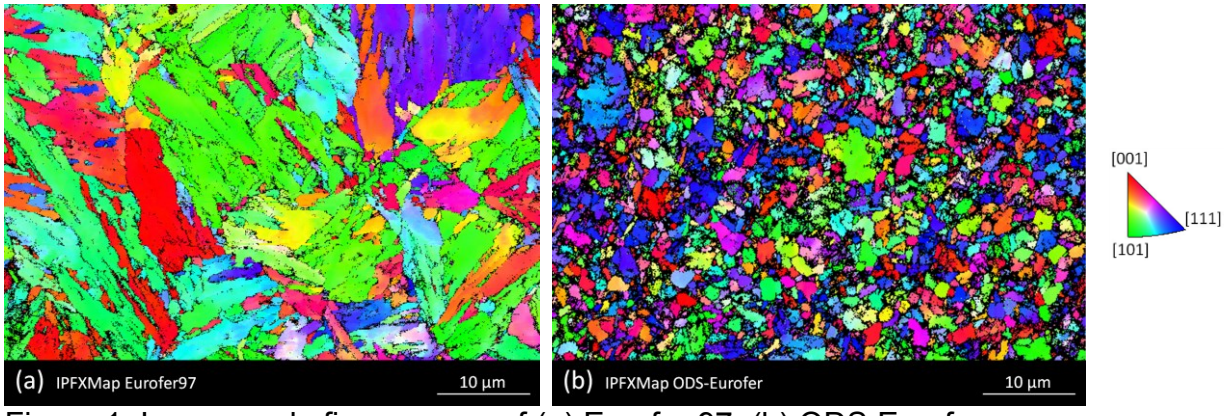

Figure 1: Inverse pole figure maps of (a) Eurofer 97, (b) ODS Eurofer.

The oxide nanoparticles dispersed in ODS Eurofer were characterized by means of small-angle neutron scattering (SANS) [17]. Eurofer 97 was taken as reference.

The mean grain size obtained from EBSD maps (minimum misorientation angle 10°), the characteristics of the particle distribution, and the Vickers hardness, HV10, of the as-received unirradiated conditions of Eurofer 97 and ODS Eurofer are summarized in Table 2. These data confirm that ODS Eurofer provides more specific grain boundary area and more specific particle-matrix interface area as potential He/defect traps or sinks. Hall-Petch and particle hardening are consistent with higher HV10.

Table 2 Basic characteristics of the as-received unirradiated conditions of Eurofer 97 and ODS-Eurofer.

Material	EBSD grain size (µm)	Particle number density (10^{22} m^{-3})	Mean particle radius (nm)	Vickers hardness HV10
Eurofer 97	2	w/o	w/o	302 ± 2
ODS Eurofer	0.5	11.5	3.8	350 ± 3

2.2 Helium-ion irradiation and microscopy

Multiple use was made of the Carl Zeiss microscopy system ORION NanoFab for the purposes of He-ion irradiation, post-irradiation microscopy and in-situ irradiation microscopy. This system will be referred to as He-ion microscope (HIM) below. A He-ion energy of 30 keV and the scanning mode were used for all experiments. The temperature was 30 ºC.

The materials were irradiated in two sets of experiments. The first set was aimed at visualizing irradiation-induced changes directly in the HIM using the video mode. After some trials, square areas of 2.5 µm x 2.5 µm of the samples were exposed to a fluence of 2 x 10^{18} He ions/cm^2.

In the second set of experiments, square areas of 5 µm x 5 µm of the samples were exposed to lower, more application-relevant fluences in the range from 10^{14} to 10^{17} He ions/cm^2. In order to facilitate post-irradiation nanoindentation experiments, special arrangements of the areas to be irradiated were pre-selected according to Fig. 2.

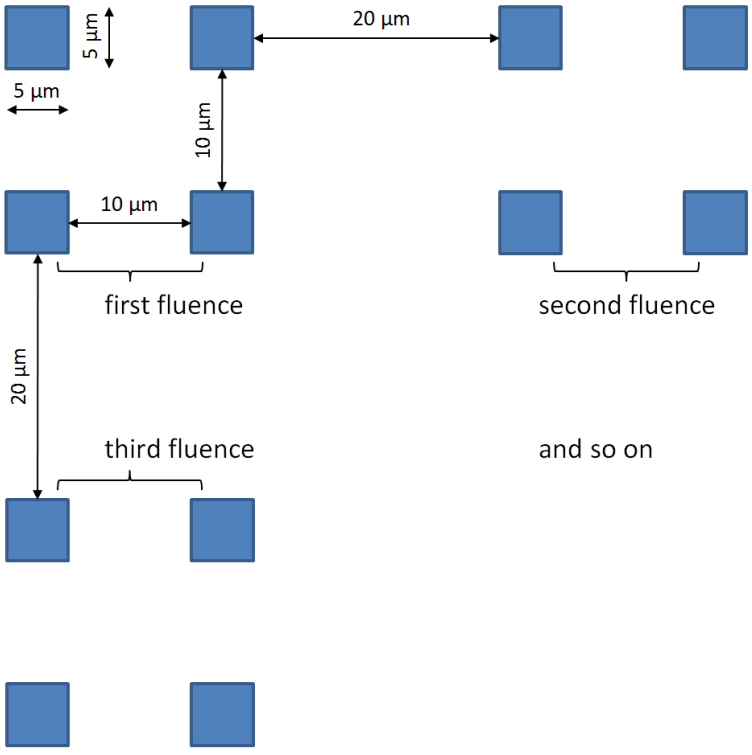

Fig. 2 Arrangement of irradiated square areas on the sample surface.

The Kinchin-Pease option of the SRIM-2008.04 binary collision code was used in order to calculate the dpa and appm-He profiles. The profiles are shown in Fig. 3 for

the case of an ion fluence of 10^{17} ions/cm^2. The profiles scale linearly with the ion fluence. The whole set of irradiation conditions is summarized in Table 3. The appm He/dpa ratio is 3 x 10^4 in all cases. It is important to note that this is much higher than the ratios between 1 and 100 more typical for applications in fusion, Generation-IV fission or transmutation devices.

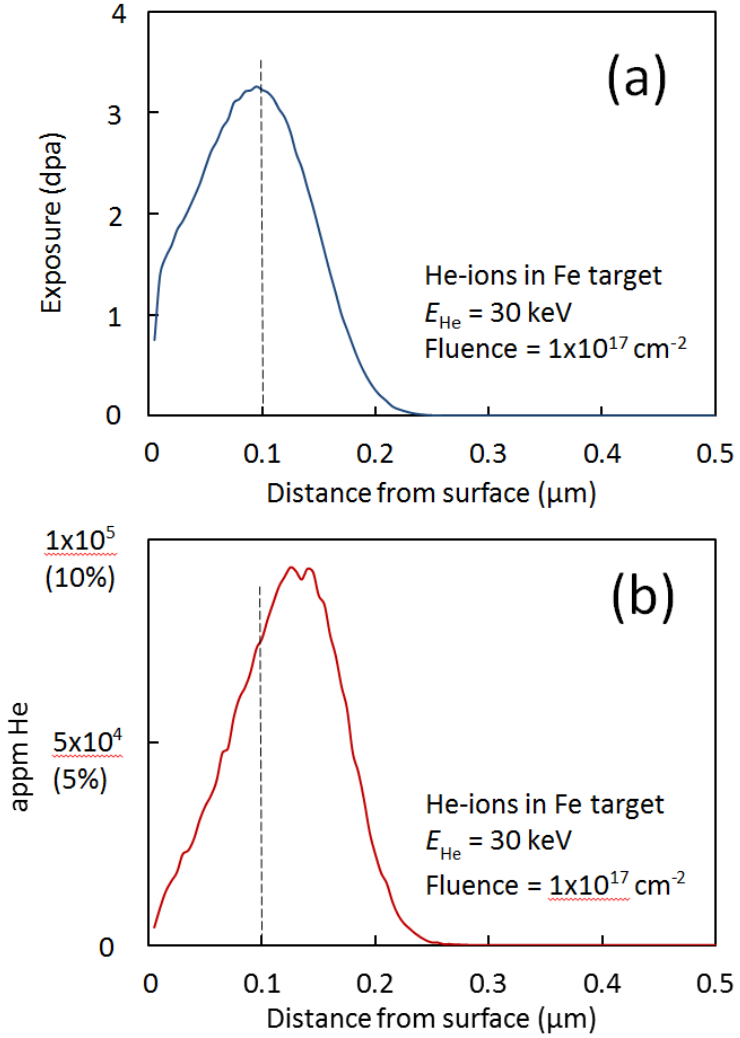

Fig. 3 Calculated profiles of (a) displacement damage and (b) appm He for the case of 10^{17} He ions/cm^2.

Table 3 Applied and SRIM-calculated irradiation parameters

Fluence (ions/cm^2)	Maximum dpa level	Maximum He concentration (%)	Area (µm x µm)	Number of irrd. areas	Purpose
2 x 10^{18}	65	180	2.5 x 2.5	1	in-situ HIM
1 x 10^{14}	0.003	0.009	5 x 5	4	post-irr. NI
3 x 10^{14}	0.01	0.03	5 x 5	4	post-irr. NI
1 x 10^{15}	0.03	0.09	5 x 5	4	post-irr. NI
3 x 10^{15}	0.1	0.3	5 x 5	4	post-irr. NI
1 x 10^{16}	0.3	0.9	5 x 5	4	post-irr. NI

3×10^{16}	1	3	5 x 5	4	post-irr. NI
1×10^{17}	3	9	5 x 5	4	post-irr. NI

2.3 Nanoindentation

Nanoindentation testing was performed using the Universal Nanomechanical Tester (UNAT, Advanced Surface Mechanics GmbH, now Zwick GmbH) equipped with a Berkovich indenter. Triples of indents with a maximum load of 500 mN were introduced prior to irradiation in order to define the absolute coordinate system for HIM and post-irradiation nanoindentation testing. For the latter, square arrays with spacings of 2 µm and maximum loads of 2 mN corresponding to indentation depths of approximately 0.1 µm were selected and kept throughout the study. The indentation depth of 0.1 µm is highlighted in Fig. 3. The square arrays of nanoindents were selected sufficiently large to cover several irradiated areas within one run and, simultaneously, sufficiently small for measuring times in access of about 24 hours and memory overflow to be avoided.

It is important to note that small but unavoidable lateral drifts during the sets of both ion irradiations and nanoindentations give rise to unforeseeable lateral configurations between irradiated areas and nanoindents. As easily deduced from the scheme in Fig. 4(a), a minimum of 4 and a maximum of 9 indents are contained inside the irradiated areas for the selected array parameters. Moreover, the irradiated areas, although visible in the HIM due to sputtering effects, cannot be seen in the optical branch of the nanoindentation device. Therefore, it was necessary to develop a strategy for the post-indentation identification of those indents belonging to the unirradiated or irradiated regions. Among the three candidate options, namely

- post-indentation identification of square arrays of smaller indents in the scanning electron microscope (see Fig. 4(b)) and separate analysis of indents clearly belonging to either irradiated or unirradiated areas,
- image correlation of nanohardness contour plots and the scheme displayed in Fig. 2 (see Fig. 4(c)),
- and identification of the indents and irradiated areas simultaneously by means of post-indentation HIM,

the first two options were applied.

All the nanoindentation runs were launched either at the same day as the corresponding ion irradiation or at the following day. In one case, an additional nanoindentation run was performed 7.5 days after the irradiation under otherwise identical conditions.

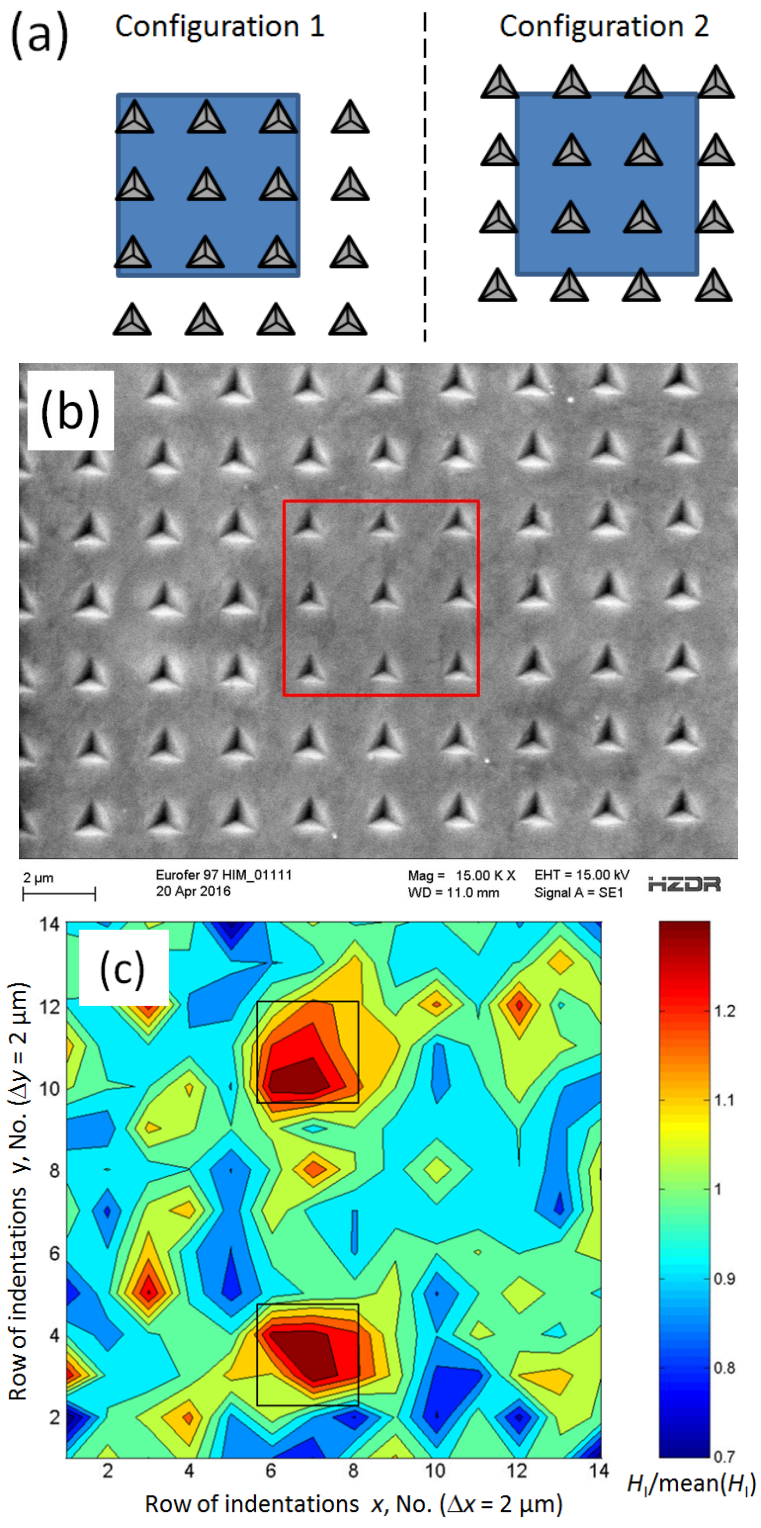

Fig. 4 (a) Limiting configurations of indentations (spacing 2 µm) versus irradiated square areas (width 5 µm), (b) SEM image of an array of indentations covering an irradiated area indicated as red square, (c) contour plot of measured nanohardness covering two irradiated square areas indicated as red squares.

3 Results

Snapshots of the in-situ irradiation experiments in the HIM up to 2 x 10^{18} He ions/cm^2 are shown in Fig. 5. Video files are provided in the supplementary material. We have observed that the onset of blistering takes place slightly above a fluence of 5 x 10^{17} He ions/cm^2 for Eurofer 97 and slightly below for ODS Eurofer. Blistering is accompanied by the formation of surface cracks through which part of the implanted He escapes. Blistering and crack formation are not in the focus of the study. The differences between Eurofer 97 and ODS Eurofer with respect to these phenomena are considered to be not significant on the basis of the available results.

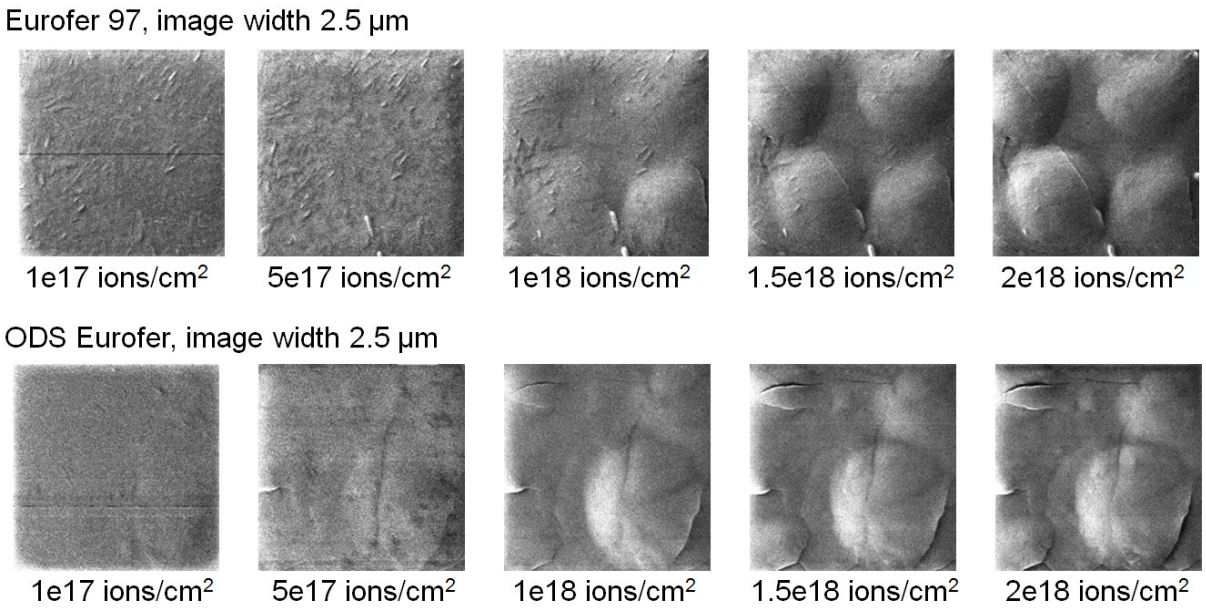

Fig. 5 Snapshots of the irradiated sample area in increments of increasing fluence for Eurofer-97 and ODS Eurofer.

For the nanoindentation experiments, the fluence range from 10^{14} to 10^{17} He ions/cm^2 was selected. The lower limit is a kind of minimum possible fluence under the present conditions, the upper limit was chosen to exclude excessive He concentrations and blistering. The results of the nanohardness measurements are plotted in Fig. 6 as function of the He-ion fluence. The mean values and standard deviations obtained for the unirradiated conditions of both materials are indicated as horizontal lines and bands, respectively. The ranking of the results is consistent with the ranking of the Vickers hardness numbers given in Table 2. The mean values and standard deviations obtained for the irradiated conditions are indicated as symbols with error bars. It is found that irradiation hardness tends to increase as a function of fluence for both materials. At the highest fluence, the difference between irradiated and unirradiated conditions is significant. The differences between Eurofer 97 and ODS Eurofer are insignificant for each fluence individually. However, a pronounced

trend towards a larger ion-irradiation-induced increase and an earlier (at lower fluence) onset of the increase for Eurofer 97 is observed on the basis of the full set of data.

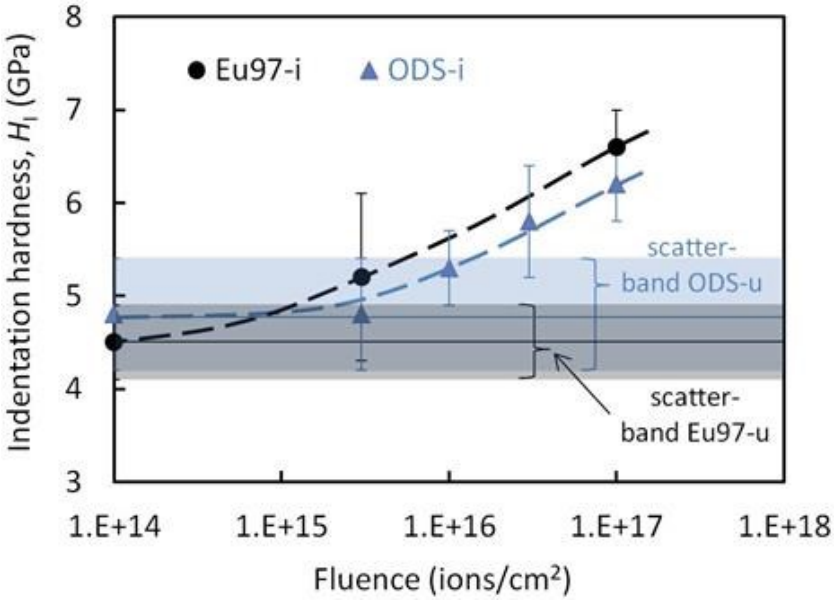

Fig. 6 Fluence dependence of indentation hardness for He-ion-irradiated Eurofer 97 and ODS Eurofer with scatter bands for the unirradiated conditions indicated.

The results obtained in the repeated irradiation/nanoindentation experiment are summarized in Table 4. For the unirradiated material, the indentation hardness obtained from the original measurement was confirmed. For the irradiated material, however, a significant reduction of the irradiation-induced hardness increase was observed.

Table 4 Indentation hardness of Eurofer 97 for different times elapsed between irradiation and indentation

Sample area (Eurofer 97)	H_I (GPa)	
	measured appr. 1.5 days after irradiation	measured appr. 7.5 days after irradiation
unirradiated reference	4.5 ± 0.4	4.4 ± 0.3
irradiated, 10^{17} ions/cm^2	6.6 ± 0.4	5.3 ± 0.3

4 Discussion

4.1 Bias

In order to prevent the results from being overstressed, the starting point of the discussion should be a consideration of bias. With respect to nanoindentation, there are three sources:

As found in Table 4, the indentation hardness depends on the time elapsed between He-ion irradiation and nanoindentation. This observation can be rationalized in terms of He diffusion at room temperature towards the free surface and the resulting loss of availability of He for hardening. A very rough and purely empirical fit of the type $H_I = H_{I0} \exp(-t/t_d)$ would yield an indentation hardness at the end of irradiation, H_{I0}, of approximately 7.2 GPa and a time constant, t_d, of the order of 6 days. This means that the results plotted in Fig. 6 are lower bounds for the real hardness at the end of irradiation and that the bias depends on the time elapsed between irradiation and indentation with variations within a few tenths of GPa in the present study. The time dependence of hardness was not in the focus of this study. However, on the basis of the experience gained here, the time dependence should be considered in future work already in the stage of experiment design.

Another source of bias is related to the depth of indentation relative to the depth profiles of implanted He and dpa, Fig. 3. It is obvious that the measured indentation hardness is a compound value of the unirradiated (softer) substrate and the irradiated (harder) layer and that it, again, represents a lower bound of the real hardness in a depth region close to maximum exposure. As both He-ion energy and indentation load were kept constant throughout the study, comparisons of hardness for different fluences are not affected. Moreover, the indentation hardness (and, therefore, indentation depth at a given load) of unirradiated Eurofer 97 and ODS Eurofer are fairly close meaning that both materials can also be compared.

Finally, the spacing of the indents is slightly smaller than required to exclude interactions between adjacent indents. (A larger spacing, say by a factor of two, would have required HIM beam times longer by a factor of four.) As indentations at the outer boarder of an array were excluded from the analysis, each analysed indentation “feels” the same environment meaning that comparisons within the study are not biased by this effect.

In summary, bias in the present study should be of some but minor importance with respect to time effects and negligible with respect to depth and spacing. However, any comparison with published absolute hardness values is out of question.

4.2 Irradiation-induced hardening

Consideration of the whole data set on the fluence dependence of indentation hardness, Fig. 6, indicates that

- there is a significant irradiation-induced hardening at sufficiently high fluence for both materials,
- the onset of significant hardening tends to occur at lower fluence for Eurofer 97,
- the irradiation- induced hardness increase is higher for Eurofer 97.

The most obvious potential reason for these findings is the formation and evolution of He bubbles, the latest stage of which was directly observed here in terms of blistering, Fig. 5. Indeed, bubble formation and related hardening of f/m and ODS 9%Cr steels was reported in previous work [15,18,19]. Henry et al. [18] observed a yield stress increase in the He-ion-irradiated (E_{He} = 23 MeV, T = 250 ºC, 0.5 at% He) 9%Cr steel T91 by more than 100% and attributed this increase to He bubbles observed by means of TEM. Roldan et al. [19] found an increase of indentation hardness in He-ion-irradiated (E_{He} = 2 to 15 MeV, T = 70 ºC, 0.075 at% He) Eurofer 97 by 41%. Heintze et al. [15] did not find a significant increase of indentation hardness in He-ion-irradiated (E_{He} = 500 keV, 300 ºC, 0.01 at% He) Eurofer 97, insignificant meaning less than 4%. This body of evidence is qualitatively consistent with the present results for Eurofer 97.

However, it seems that the hardening observed by Henry et al. [18] and Roldan et al. [19] is higher than indicated by the trend line for Eurofer 97 in Fig. 6. This cannot be sufficiently explained by the underestimation of hardening due to the bias discussed above. An additional influence factor is based on the relationship between He-ion energy and the number of displacements per injected He atom. The latter exhibits a (weaker than linear) increase with increasing energy. As the He-ion energies are higher in the above-mentioned studies [15,18,19], the synergism between He injection and displacement damage should also be stronger and ascend in the order of ion energies. This was clearly shown in [15] on the basis of the indentation hardness increase due to single-beam Fe-ion (5 dpa), He-ion (100 appm) and dual-beam (5 dpa, 100 appm) irradiations. Indeed, there it was found that $\Delta H_{He} << \Delta H_{Fe+He} - \Delta H_{Fe}$.

As for the comparison of Eurofer 97 versus ODS Eurofer, the present observations indicate that the presence of oxide nanoparticles (Table 2) is efficient to reduce the detrimental effect of He. This is consistent with an increasing body of reported evidence mainly based on single-beam He irradiation [4,5,12,15,19-23]. The most striking evidence in the present context is perhaps related to the observation of nano-bubbles that preferentially form at the interface between Fe matrix and Y_2O_3 particles in a model system also irradiated with He-ions in a He-ion microscope [12]. The present findings indicate that this effect is dominant in ODS Eurofer below a certain threshold of the order of magnitude of 0.1 at% He. After the threshold is exceeded, the hardness increases at about the same rate as for Eurofer 97 but with the lower absolute level maintained. The threshold might be related to the exhaustion of the available particle-matrix interface as trapping sites for He.

A second potential reason for the observed irradiation-induced hardness increase is the displacement-damage-induced point defect formation and their effect on the microstructure evolution. Indeed, neutron- and ion-irradiation-induced formation of dislocation loops [24-26] and α'-phase particles [27-30] was reported in Fe-9%Cr-based alloys. While oxide particle-matrix interfaces seem to be inefficient as point-defect sinks [15], grain boundaries are. They may either act as point-defect sinks or as interstitial atom traps to reemit interstitials and enhance vacancy-interstitial recombination [31]. However, no loops were observed by means of TEM after 23 MeV-He-ion irradiation of T91 up to 0.8 dpa [18]. The volume fraction of α' (if any) should also be small because of the weak supersaturation in 9% Cr alloys with a solubility limit of Cr close to 9% [32,33]. Moreover, α'-phase particles were reported to be weak obstacles for dislocation glide [34]. Therefore, we assume that the dpa-component of the He-ion irradiation is a secondary source of both the hardening observed for both alloys and the surplus of hardening observed for Eurofer 97 over ODS Eurofer under the present irradiation conditions. Hence, the present findings are primarily caused by the populations of He bubbles.

4.3 Technical comment on He-ion irradiation

From the viewpoint of methodology, the application of HIM displays a number of pros and cons, some of which can be deduced from the appm He versus dpa map shown in Fig. 7. This map summarizes selected irradiation experiments including single-beam He ions (Henry 2003 [18], Heintze 2016 [15], Edmondson 2013 [35], Liu 2016 [36]), single-beam Fe ions (Toloczko 1994 [37], Lee 1999 [38], Heintze 2016 [15]), dual-beam He/Fe ions (Lee 1999 [38], Ando 2004 [39], Heintze 2016 [15]) and neutrons (Matijasevic 2008 [24]) reported in the literature for f/m and ODS steels. The HIM irradiations of the present study constitute the upper bound of the covered field. Acceleration of the He ions to higher energies, e.g. 23 MeV [18], give rise to relatively minor shifts towards higher dpa levels. Neutron and self-ion irradiations constitute the lower bound of the covered field. In this kind of experiments, He injection is typically ignored, although some transmutation He may appear. In the map, we assume 1 appm He instead of zero for the purpose of logarithmic axis disposition. Dual beam irradiations potentially are capable of filling the whole area between lower and upper bound by way of adjusting the the He/Fe ion flux ratio. The black lines indicate the loci corresponding to appm He/dpa ratios of 1, 10 and 100, which are considered to be representative of fission and fusion reactor components and spallation source windows, respectively. Finally, He produced by tritium decay (dot-and-dashed line) is unique in that no radiation damage occurs [40]. In the map, we assume 10^{-3} dpa instead of zero for the purpose of logarithmic axis disposition. It is important to note that temperature does matter in He effects but is not specified in Fig. 7.

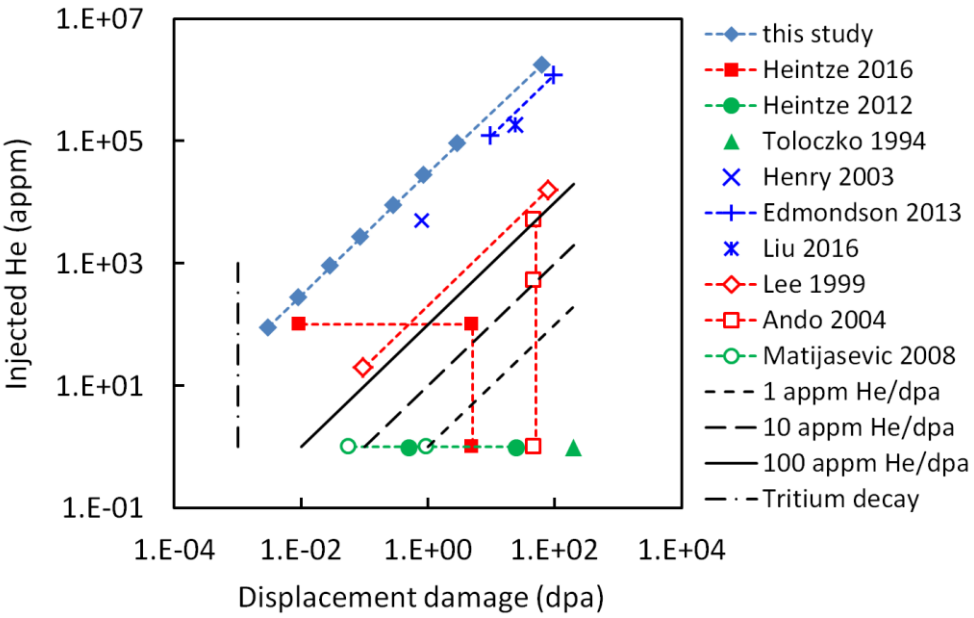

Fig. 7 Maps of injected He versus displacement damage for the present HIM irradiations, reported single-beam He-ion, Fe-ion and dual beam accelerator-besed irradiations and neutron-irradiations, and application-relevant irradiation conditions, for references see text.

It turns out that, except for the case of tritium decay, HIM irradiations are relatively far from the application-relevant field, which causes a transferability issue if the objective of a study is to mimic those application-relevant irradiation conditions. However, this is not a major issue as long as irradiations serve as a means for basic research, e.g. in order to expand the observation window in terms of appm He/dpa ratios, explore new irradiation effects or intentionally provoke bubble formation. It is interesting to note that the whole set of irradiation conditions of the present study (full diamonds in Fig. 7) can be realized within a single properly pre-designed HIM run of several hours rather than a day.

Another issue is related to the penetration depth of ions. The appm He/dpa ratio can be tuned within certain limits (see Fig. 7) by changing the He-ion energy. However, changes of the ion energy give rise to changes of the average penetration depth of He ions with consequences for nanoindentation testing. A balance between the depth profile of appm He and the indentation process (taking into account the plastic zone) is clearly required with respect to the irradiation effect, the indentation size effect and the effect of the unirradiated substrate. Moreover, the ratio between indentation depth and size is fixed meaning that the balance between indentation size, indentation spacing (including measuring time), size of the irradiated areas (including irradiation time) and microstructural length scales comes into play. The present experiments represent a tentative trade-off between all these factors on the basis of HIM irradiations and indentations into the irradiated surface. Options to avoid certain issues are He-ion irradiations with stepwise changes of the ion energy to flatten the

profile [19] and investigations of cross sections through the irradiated profile [35,36]. Dual-beam He-/Fe-ion irradiations pose an alternative option for almost free variations of appm He/dpa ratios (see Fig. 7). The role of HIM is to complement such dual beam irradiations rather than replacing them.

Finally, it is important to emphasize the lateral resolution of HIM with respect to both irradiation and imaging, which opens the door for experiments hardly feasible in accelerator-based irradiations. Sample heating in the HIM has become available. Nanoindentation in the HIM would also be useful in the present context but is not yet available.

5 Conclusions

Imaging and He-ion irradiation in the He-ion microscope at 30 ºC in a wide range of appm He (from 0.9 x 10^2 to 1.8 x 10^6) and displacements per atom (from 3 x 10^{-3} to 65) were combined with post-irradiation nanoindentation in order to detect blistering and irradiation-induced hardness changes. We have found that the combination of techniques

(1) is suitable to provoke and detect irradiation-induced hardness changes and blistering,
(2) exhibits special advantages such as an efficient coverage of a wide range of He-ion fluence, the adequacy of small sample areas, reasonably short irradiation times, or the possibility of site-specific irradiations.

The results indicate that

(3) the irradiation-induced hardness increase is higher and the onset of significant hardening tends to occur at lower fluence for Eurofer 97 than for ODS Eurofer,
(4) the presence of oxide nanoparticles is efficient to reduce the detrimental effect of He under the applied irradiation conditions,
(5) there is a decrease of hardness with increasing time elapsed after the irradiation on the time-scale of days due to the escape of He through the sample surface.

Factors of experimental bias as well as the classification of HIM irradiations within the sets of reported irradiations and application-relevant irradiation conditions were discussed.

Acknowledgement

Access to the Ion Beam Center (IBC) of the HZDR is gratefully acknowledged. This work contributes to the Joint Programme on Nuclear Materials (JPNM) of the European Energy Research Alliance (EERA). The authors express their gratitude to Peter Hosemann for discussions.

Appendix A. Supplementary data

Supplementary data related to this article (video files related to Fig. 5) can be found at

References

[1] R.S. Barnes, Nature 206 (1965) 1307-1310. doi:10.1038/2061307a0
[2] H. Ullmaier, Radiation Effects 78 (1983) 1-10. doi: 10.1080/00337578308207355
[3] L.K. Mansur, A.F. Rowcliffe, R.K. Nanstad, S.J. Zinkle, W.R. Corwin, R.E. Stoller, J. Nucl. Mater. 329–333 (2004) 166–172. doi:10.1016/j.jnucmat.2004.04.016
[4] A. Möslang, T. Wiss, Nature Materials 5 (2006) 679-680. doi: 10.1038/nmat1715
[5] G.R. Odette, D.T. Hoelzer, JOM 62 (2010) 84-92. doi:10.1007/s11837-010-0144-1
[6] V. Krsjak, J. Kuriplach, T. Shen, V. Sabelova, K. Sato, Y. Dai, J. Nucl. Mater. 456 (2015) 382–388. doi: 10.1016/j.jnucmat.2014.10.014
[7] J. Knaster, A. Moeslang, T. Muroga, Nature Physics 12 (2016) 424-434. doi: 10.1038/NPHYS3735
[8] P. Vladimirov, A. Möslang, J. Nucl. Mater. 356 (2006) 287–299. doi: 10.1016/j.jnucmat.2006.05.037
[9] P. Dubuisson, Y. de Carlan, V. Garat, M. Blat, J. Nucl. Mater. 428 (2012) 6–12. doi:10.1016/j.jnucmat.2011.10.037
[10] N.P. Economou, J.A. Notte, W.B. Thompson, Scanning 33 (2011) 1-7. doi: 10.1002/sca.20239
[11] G. Hlawacek, V. Veligura, R. van Gastel, B. Poelsema, J. Vac, Sci. Technol. B 32 (2014) 020801. doi: 10.1116/1.4863676
[12] T.C. Kaspar, M.E. Bowden, C.M. Wang, V. Shutthanandan, N.R. Overman, R.M. van Ginhoven, B.D. Wirth, R.J. Kurtz, J. Nucl. Mater. 457 (2015) 352–361. doi: 10.1016/j.jnucmat.2014.11.046
[13] Z.-J. Wang, F.I. Allen, Z.-W. Shan, P. Hosemann, Acta Mater. 121 (2016) 78-84. doi: 10.1016/j.actamat.2016.08.085
[14] F. Tavassoli, Fusion Demo Interim Structural Design Criteria (DISDC) - Appendix A Material Design Limit Data A3.S18E Eurofer Steel, DMN Technical Report, DMN/DIR/NT/2004-02/A TW4-TTMS-005-D01, 2004.
[15] C. Heintze, F. Bergner, M. Hernandez-Mayoral, R. Kögler, G. Müller, A. Ulbricht, J. Nucl. Mater. 470 (2016) 258-267. doi: 10.1016/j.jnucmat.2015.12.041
[16] R. Lindau, A. Möslang, M. Schirra, P. Schlossmacher, M. Klimenkov, J. Nucl. Mater. 307–311 (2002) 769–772. doi: 10.1016/S0022-3115(02)01045-0
[17] C. Heintze, F. Bergner, A. Ulbricht, M. Hernández-Mayoral, U. Keiderling, R. Lindau, T. Weissgärber, J. Nucl. Mater. 416 (2011) 35–39. doi: 10.1016/j.jnucmat.2010.11.102
[18] J. Henry, M.-H. Mathon, P. Jung, J. Nucl. Mater. 318 (2003) 249–259. doi:10.1016/S0022-3115(03)00118-1
[19] M. Roldán, P. Fernández, J. Rams, D. Jiménez-Rey, E. Materna-Morris, M. Klimenkov, J. Nucl. Mater. 460 (2015) 226–234. doi: 10.1016/j.jnucmat.2015.02.025

[20] J. Chen, P. Jung, J. Henry, Y. de Carlan, T. Sauvage, F. Duval, M.F. Barthe, W. Hoffelner, J. Nucl. Mater. 437 (2013) 432–437. doi: 10.1016/j.jnucmat.2013.02.071
[21] A.I. Ryazanov, O.K. Chugunov, S.M. Ivanov, S.T. Latushkin, R. Lindau, A. Möslang, A.A. Nikitina, K.E. Prikhodko, E.V. Semenov, V.N. Unezhev, P.V. Vladimirov, J. Nucl. Mater. 442 (2013) S153–S157. doi: 10.1016/j.jnucmat.2013.03.080
[22] S. Chen, Y. Wang, K. Tadaki, N. Hashimoto, S. Ohnuki, J. Nucl. Mater. 455 (2014) 301–305. doi: 10.1016/j.jnucmat.2014.06.041
[23] W.B. Liu, Y.Z. Ji, P.K. Tan, C. Zhang, C.H. He, Z.G. Yang, J. Nucl. Mater. 479 (2016) 323-330. doi: 10.1016/j.jnucmat.2016.07.030
[24] M. Matijasevic, E. Lucon, A. Almazouzi, J. Nucl. Mater. 377 (2008) 101–108. doi: 10.1016/j.jnucmat.2008.02.063
[25] M. Matijasevic, A. Almazouzi, J. Nucl. Mater. 377 (2008) 147–154. doi: 10.1016/j.jnucmat.2008.02.061
[26] M. Hernández-Mayoral, C. Heintze, E. Oñorbe, J. Nucl. Mater. 474 (2016) 88-98. doi: 10.1016/j.jnucmat.2016.03.002
[27] M.H. Mathon, Y. de Carlan, G. Geoffroy, X. Averty, A. Alamo, C.H. de Novion, J. Nucl. Mater. 312 (2003) 236–248. doi:10.1016/S0022-3115(02)01630-6
[28] C. Heintze, F. Bergner, A. Ulbricht, H. Eckerlebe, J. Nucl. Mater. 409 (2011) 106–111. doi:10.1016/j.jnucmat.2010.09.010
[29] V. Kuksenko, C. Pareige, P. Pareige, J. Nucl. Mater. 432 (2013) 160–165. doi: 10.1016/j.jnucmat.2012.07.021
[30] O. Tissot, C. Pareige, E. Meslin, B. Décamps, J. Henry, Mater. Res. Lett. (2016) 1-7. doi: 10.1080/21663831.2016.1230896
[31] X.-M. Bai, A.F. Voter, R.G. Hoagland, M. Nastasi, B.P. Uberuaga, Science 327 (2010) 1631-1634. doi: 10.1126/science.1183723
[32] G. Bonny, D. Terentyev, L. Malerba, Scripta Mater. 59 (2008) 1193–1196. doi: 10.1016/j.scriptamat.2008.08.008
[33] F. Bergner, A. Ulbricht, C. Heintze, Scripta Mater. 61 (2009) 1060–1063. doi: 10.1016/j.scriptamat.2009.08.028
[34] F. Bergner, C. Pareige, M. Hernández-Mayoral, L. Malerba, C. Heintze, J. Nucl. Mater. 448 (2014) 96–102. doi: 10.1016/j.jnucmat.2014.01.024
[35] P.D. Edmondson, C.M. Parish, Y. Zhang, A. Hallén, M.K. Miller, J. Nucl. Mater. 434 (2013) 210–216. doi: 10.1016/j.jnucmat.2012.11.049
[36] W.B. Liu, Y.Z. Ji, P.K. Tan, C. Zhang, C.H. He, Z.G. Yang, J. Nucl. Mater. 479 (2016) 323-330. doi: 10.1016/j.jnucmat.2016.07.030
[37] M.B. Toloczko, F.A. Garner, C.R. Eiholzer, J. Nucl. Mater. 212-215 (1994) 604-607. doi:10.1016/0022-3115(94)90131-7
[38] E.H. Lee, J.D. Hunn, G.R. Rao, R.L. Klueh, L.K. Mansur, Journal of Nuclear Materials 271-272 (1999) 385-390. doi: 10.1016/S0022-3115(98)00722-3
[39] M. Ando, E. Wakai, T. Sawai, H. Tanigawa, K. Furuya, S. Jitsukawa, H. Takeuchi, K. Oka, S. Ohnuki, A. Kohyama, J. Nucl. Mater. 329–333 (2004) 1137–1141. doi: 10.1016/j.jnucmat.2004.04.290
[40] D.E. Rawl, G.R. Caskey, J.A. Donovan, Low-temperature Helium embrittlement of Tritium-charged stainless steel, paper presented at the 109th Annual AIME Meeting, Las Vegas, 1980.